AIMETA 2017
XXIII Conference
The Italian Association of Theoretical and Applied Mechanics
Luigi Ascione, Valentino Berardi, Luciano Feo, Fernando Fraternali and Antonio Michele Tralli (eds.)
Salerno, Italy, 4–7 September 2017

FLUID-SOLID-ELECTRIC STABILITY ANALYSIS AND PASSIVE CONTROL OF A PIEZOELECTRIC FLEXIBLE PLATE CLAMPED ON A RIGID CYLINDER

Marco Carini, Jean-Lou Pfister and Olivier Marquet

ONERA - DAAA
8 Rue des Vertugadins, 92190, France
e-mail: marco.carini@onera.fr
jean-lou.pfister@onera.fr
olivier.marquet@onera.fr

Keywords: fluid-structure instabilities, piezoelectric shunts, global stability analysis

Abstract. *We investigate the passive control of a flutter instability arising for an elastic plate clamped at the rear of a rigid cylinder immersed in a low Reynolds number flow. Shunted piezoelectric patches are placed on the elastic plate and used to suppress or reduce the deformation of the plate. A classical Arbitrary Lagrangian Eulerian formulation (ALE) is used to describe the coupled fluid-structure dynamics with a monolithic approach. The passive control problem is here addressed by performing a linear stability analysis of the fully coupled fluid-solid-electric problem. For the values of the non-dimensional parameters investigated - Reynolds number* $Re = 80$*, bending stiffness* $K = 0.3$ *and solid/fluid density ratio* $\rho = 50$ *- the modal stability analysis of the fluid-structure configuration shows the existence of an unstable oscillating mode, responsible for the onset of the plate deformation. By connecting the piezoelectric patches to a simple resistive shunt circuit, this mode can be stabilized for a finite range of electrical resistance* R_e *values. The dependence of the stability properties of the fluid-solid-electric system on the piezoelectric and shunt-circuit parameters is investigated and the physical mechanisms underlying the suppression of the unstable mode are analysed.*

1 INTRODUCTION

Piezoelectric materials are widely employed in industrial engineering, where their properties of coupling mechanical stresses and strains with an electric field are essentially exploited to detect, measure and control structural vibrations. In such case, the 'inverse piezoelectric effect', which refers to the deformation of the piezoelectric material that results from the application of an electric field, is used to reduce or even suppress the mechanical vibrations. Efficient numerical formulations for modelling piezoelectric elements embedded in an elastic structure [1] have been developed and the effect of connecting the piezoelectric patches to an electric-circuit has been assessed for vibration reduction [2]. These numerical formulations were only developed for modelling the electro-mechanical coupling.

In recent years, the 'direct piezoelectric effect', which refers to a change in the electric polarization that is produced in certain materials when they are subjected to mechanical stresses, has attracted research on energy harvesting. Relying on this effect, an active research field has investigated the potential of producing electrical energy from flow-induced deformations of elastic structures. The deformation of flexible membranes induced by the vortex-shedding wake of bluff-bodies [3, 4] or the spontaneous flapping of flexible flags into an axial flow [5] are two canonical fluid-structure configurations investigated for energy harvesting. Most of the previous theoretical and numerical studies on the flapping of piezoelectric flags have considered idealized fluid inviscid models. In a recent numerical study [6] aiming at identifying the critical non-dimensional parameters governing the response of piezoelectric beams fluttering in viscous flow, time-marching simulations of the nonlinear fluid-solid-electric coupled problem were performed. The determination of the nonlinear response is mandatory to assess the overall efficiency of the system to harvest energy. However, when considering passive control problems aiming at suppressing flow oscillations [8, 7], the determination of the linearised response of the controlled system is sufficient to assess the control efficiency. By computing the neutral curve in the space of governing non-dimensional parameters, one can distinguish between unstable and stable regions, the latter being regions for which the control is efficient in suppressing the deformation of the elastic structure.

Linear stability analysis of fluid-solid-electric configurations have been investigated for purely inviscid flow model [9], which is a reasonable approximation of the flow dynamics for piezoelectric flags in high Reynolds number flows. However, when considering more complex flow configurations, such as a flexible plate clamped at the rear of a rigid cylinder immersed in a uniform flow [10], the flow separation on the rigid cylinder precludes us from using purely inviscid models. The first objective of the present study is to present the formalism for a linear stability analysis of fluid-solid-electric system where the flow is modelled by the incompressible Navier-Stokes equations. To account for the coupling between the Eulerian fluid motion and the Lagrangian deformation of the elastic solid, we adopt the Arbitrary Lagrangian Eulerian framework, a conformal method that has the advantage to accurately describe the fluid/structure interface compared to nonconformal approaches as the Immersed Boundary Method [20]. To our knowledge, the formalism for investigating the linear stability analysis of fluid/structure interaction in the ALE framework has been first proposed in [11, 12]. In the present paper, we extend this analysis to take into account the coupling with piezoelectric patches, modelled following [1]. We investigate the passive control of a flexible plate attached at the rear of a rigid cylinder immersed in a viscous flow, by means of piezoelectric patches embedded in the elastic structure.

The paper is organized as follows. The configuration and the mathematical modelling of the

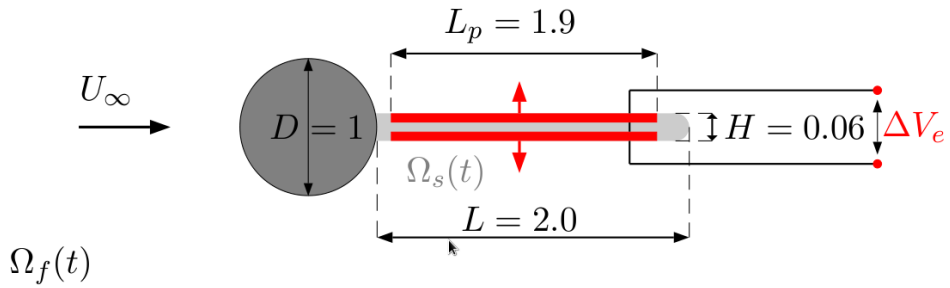

Figure 1: Sketch of the geometrical configuration with a rigid cylinder (dark grey area) and an elastic splitter plate (light grey area) equipped with two piezoelectric patches (red area). The patches are connected in parallel with opposite poling direction (red arrows).

fluid, of the elastic structure and of the piezoelectric patches are detailed in Section 2, where the linear stability analysis of the fluid-solid-electric system is also introduced. The numerical approaches, including the spatial discretisation with finite elements and the numerical algorithms used for the stability analysis are exposed in Section 3. Results of the stability analysis are shown in Section 4. The instability of the uncontrolled fluid/structure configuration is first analysed. The effect of adding piezoelectric patches on the elastic plate is then investigated by considering an open-circuit configuration. Finally, results of passive control are shown by considering a resistive-shunted configuration, obtained by connecting the two piezoelectric patches with an electric resistance. The effect of varying the electric resistance on the stabilization of fluid-structure mode and the change in the mode selection are presented.

2 MATHEMATICAL MODEL

2.1 Configuration

The fluid-structure configuration investigated in the present study is sketched in Figure 1. An elastic plate (light grey) is clamped at the rear of a rigid cylinder (dark grey) immersed in a upstream uniform flow of velocity U_∞. To control the deformation, two piezoelectric patches (red) are embedded at the top and bottom sides of the elastic plate. All the lengths are made non-dimensional by means of the cylinder diameter D and the non-dimensional sizes of these elements are indicated in the Figure 2. Due to the motion of the elastic plate, the fluid $\Omega_f(t)$, elastic solid $\Omega_s(t)$ and piezoelectric $\Omega_p(t) = \Omega_p^t(t) \cup \Omega_p^t(t)$ domains deform with time t. $\Omega_p^t(t)$ and $\Omega_p^b(t)$ indicate the top and bottom patches, respectively, as illustrated in Figure 2. In order to account for the coupling between the fluid, the elastic plate and the piezoelectric patches for numerical implementation, the Arbitrary Eulerian Lagrangian formalism is adopted [14]. For conciseness, the formalism is introduced by considering a fluid/structure configuration without piezoelectric patches. In the following, the latter can be treated as the elastic structure, without loss of generality. Let us introduce the *reference undeformed configurations*, denoted Ω_s^r and Ω_f^r, which correspond to the stress-free solid configuration and the corresponding surrounding fluid domain. In these time-independent configurations all the points are denoted by $\boldsymbol{X}$ while their position in the deformed configurations, $\Omega_f(t)$ and $\Omega_s(t)$, are denoted by $\boldsymbol{x}$. The mapping of the points in the deformed configuration relative to their reference position is denoted by $\boldsymbol{x}(\boldsymbol{X}, t)$. In the solid domain, this mapping is associated to the displacement of material points and leads to the classical Lagrangian description of the solid dynamics. In the fluid domain, the displacement of the points is not related to a physical equation. An arbitrary extension operator,

denoted by $\mathcal{E}$, needs to be introduced to propagate the solid material displacement of the fluid-structure interface $\Gamma_{fs}(t) = \Omega_f(t) \cap \Omega_s(t)$ into the fluid domain. The complete ALE mapping is expressed in terms of the displacement $\boldsymbol{\xi} = \boldsymbol{x} - \boldsymbol{X}$ as follows

$$\boldsymbol{\xi}(\boldsymbol{X}, t) = \boldsymbol{x}(\boldsymbol{X}, t) - \boldsymbol{X} = \begin{cases} \boldsymbol{\xi}_s & \text{on } \Omega_s^r, \\ \boldsymbol{\xi}_f = \mathcal{E}(\boldsymbol{\xi}_s|_{\Gamma_{FS}^r}) & \text{on } \Omega_f^r, \end{cases} \tag{1}$$

where we have introduced a different notation for the physical displacement of the solid material points $\boldsymbol{\xi}_s$ and the 'grid displacement' of the fluid domain points $\boldsymbol{\xi}_f$. The transformation gradient tensor $\boldsymbol{F}$ and its determinant J are defined as

$$\boldsymbol{F} = \frac{\partial \boldsymbol{x}}{\partial \boldsymbol{X}} = \boldsymbol{I} + \boldsymbol{\nabla}\boldsymbol{\xi} \quad \text{and} \quad J = \det \boldsymbol{F}, \tag{2}$$

and contain all the information related to the local deformation of the solid and fluid domains. In the present study, the extension operator $\mathcal{E}(\boldsymbol{\xi}_s|_{\Gamma_{FS}})$ is defined as a weighted Laplace operator in the reference domain

$$\boldsymbol{\nabla}\boldsymbol{\cdot}\left(\frac{1}{h^2}\boldsymbol{\nabla}\boldsymbol{\xi}_f\right) = 0 \quad \text{on } \Omega_f^r, \tag{3}$$

supplemented with the boundary conditions $\boldsymbol{\xi}_f = \boldsymbol{\xi}_s$ on Γ_{FS}^r and $\boldsymbol{\xi}_f = \boldsymbol{0}$ on $\partial\Omega_f^r/\Gamma_{FS}^r$. In the above equation $h(\boldsymbol{X})$ denotes the local mesh size which results in a selective treatment of the deformation [18].

2.2 Fluid-structure interaction modelling

The fluid flow past the solid-elastic structure is described by the incompressible Navier-Stokes equations which are written in the non-dimensional form as follows

$$\begin{aligned} \frac{\partial \tilde{\boldsymbol{u}}}{\partial t} + \tilde{\boldsymbol{\nabla}}\boldsymbol{\cdot}\left(\tilde{\boldsymbol{u}} \otimes \tilde{\boldsymbol{u}} - \tilde{\boldsymbol{\sigma}}_f(\tilde{\boldsymbol{u}}, \tilde{p})\right) &= \boldsymbol{0}, \\ \tilde{\boldsymbol{\nabla}}\boldsymbol{\cdot}\,\tilde{\boldsymbol{u}} &= 0, \end{aligned} \tag{4}$$

where $\tilde{\boldsymbol{u}} = \tilde{\boldsymbol{u}}(\boldsymbol{x}, t)$ denotes the Eulerian fluid velocity on the deformed domain $\Omega_f(t)$ and $\tilde{\boldsymbol{\sigma}}_f(\tilde{\boldsymbol{u}}, \tilde{p})$ is the total fluid stress tensor defined as

$$\tilde{\boldsymbol{\sigma}}_f(\tilde{\boldsymbol{u}}, \tilde{p}) = -\tilde{p}\boldsymbol{I} + \frac{1}{Re}\left(\tilde{\boldsymbol{\nabla}}\tilde{\boldsymbol{u}} + \tilde{\boldsymbol{\nabla}}\tilde{\boldsymbol{u}}^T\right), \tag{5}$$

with $\tilde{p} = \tilde{p}(\boldsymbol{x}, t)$ being the fluid pressure, $(\cdot)^T$ the transpose operation and $\boldsymbol{I}$ the identity tensor. The flow variables are made non-dimensional using the cylinder diameter D, the velocity U_∞ of the incoming uniform fluid stream and the constant fluid density ρ_f. The Reynolds number is then defined as $Re = U_\infty D/\nu_f$, with ν_f being the kinematic viscosity of the fluid.

To determine the Navier-Stokes equations in the reference domain, the fluid velocity $\boldsymbol{u}$ and pressure p mapped on this domain are introduced, i.e. $\boldsymbol{u}(\boldsymbol{X}, t) = \tilde{\boldsymbol{u}}(\boldsymbol{x}, t)$ and $p(\boldsymbol{X}, t) = \tilde{p}(\boldsymbol{x}, t)$. After straightforward chain rule calculus, the following equations are obtained

$$\begin{aligned} J\frac{\partial \boldsymbol{u}}{\partial t} + (\boldsymbol{\nabla}\boldsymbol{u}J\boldsymbol{F}^{-1})(\boldsymbol{u} - \boldsymbol{w}) - \boldsymbol{\nabla}\boldsymbol{\cdot}\left(J\boldsymbol{\sigma}_f(\boldsymbol{u}, p)\boldsymbol{F}^{-T}\right) &= \boldsymbol{0}, \\ \boldsymbol{\nabla}\boldsymbol{\cdot}\left(J\boldsymbol{F}^{-1}\boldsymbol{u}\right) &= 0, \end{aligned} \tag{6}$$

where $\boldsymbol{w} = \partial \boldsymbol{\xi}_f / \partial t$ is the 'grid' velocity and $\boldsymbol{\sigma}_f(\boldsymbol{u}, p)$ is the total fluid stress tensor in the reference configuration

$$\boldsymbol{\sigma}_f(\boldsymbol{u}, p) = -p\boldsymbol{I} + \frac{1}{Re}\left(\boldsymbol{F}^{-1}\boldsymbol{\nabla}\boldsymbol{u} + \boldsymbol{\nabla}\boldsymbol{u}^T\boldsymbol{F}^{-T}\right). \tag{7}$$

Note also that all the spatial derivatives are now referred to $\boldsymbol{X}$, as highlighted by the different notation of the differentiation operator, i.e. $\tilde{\boldsymbol{\nabla}} f = \partial \tilde{f} / \partial \boldsymbol{x}$ and $\boldsymbol{\nabla} f = \partial f / \partial \boldsymbol{X}$. By comparing Eqs. (6) with Eqs. (4) it is clear that the dependence on $\boldsymbol{\xi}_f$ has been made explicit at the cost of a more complicated form of the governing fluid equations due to the introduction of additional nonlinear terms of geometric nature resulting from the ALE mapping.

The dynamics of the solid structure is described by assuming a linear isotropic material under small deformations which results in the following Lagrangian equation for the solid displacement field $\boldsymbol{\xi}_s$

$$\rho \frac{\partial^2 \boldsymbol{\xi}_s}{\partial t^2} - \boldsymbol{\nabla} \cdot \boldsymbol{\sigma}_s(\boldsymbol{\xi}_s) = \boldsymbol{0}, \tag{8}$$

where $\rho_= \rho_s / \rho_f$ is the solid-to-fluid density ratio, ρ_s being the solid density. $\boldsymbol{\sigma}_s(\boldsymbol{\xi}_s)$ denotes the classical Cauchy stress tensor with

$$\boldsymbol{\sigma}_s = 2\mu_s \boldsymbol{\varepsilon} + \lambda_s Tr(\boldsymbol{\varepsilon}) \boldsymbol{I}, \tag{9}$$

where μ_s, λ_s are the Lamé coefficients of the elastic material and $\boldsymbol{\varepsilon} = (1/2)(\boldsymbol{\nabla}\boldsymbol{\xi}_s + \boldsymbol{\nabla}\boldsymbol{\xi}_s{}^T)$ is the linearised deformation tensor. In the above constitutive equation the notation $Tr(\cdot)$ has been introduced for the trace operator. Note that all the solid variables are made dimensionless using the same physical quantities employed for the fluid variables.

The fluid structure equations (6)-(8) are coupled by means of kinematic and equilibrium conditions at the Γ^r_{FS} which are given by

$$\begin{aligned} \boldsymbol{u} &= \frac{\partial \boldsymbol{\xi}_s}{\partial t}, \\ J\boldsymbol{\sigma}_f(\boldsymbol{u}, p)\boldsymbol{F}^{-T} \cdot \boldsymbol{n} &= \boldsymbol{\sigma}_s \cdot \boldsymbol{n}, \end{aligned} \tag{10}$$

where $\boldsymbol{n}$ denotes the unit normal vector to Γ^r_{FS}. The first equation states the equality of fluid and solid velocities while the second one expresses the equilibrium condition between the fluid and solid stresses at the common interface. Additional boundary conditions are introduced on the remaining portion of $\partial\Omega^r_f$ and $\partial\Omega^r_s$. In particular a no-slip condition are imposed at the boundary between the fluid and the rigid cylinder. At the boundary between the rigid cylinder and the elastic plate, a clamped condition for the elastic plate is assumed. The external fluid boundary is assumed of rectangular shape and aligned with the flow direction. On the inlet, a uniform unitary streamwise velocity profile is imposed, while a normal stress-free boundary condition is used at the outlet boundary. Finally, the symmetric conditions $\partial u / \partial y = 0$, $v = 0$ are imposed on the lateral boundaries of the fluid domain with $\boldsymbol{u} = \{u, v\}^T$, where we adopt a Cartesian reference system with its origin located on the cylinder centre and with the x-axis aligned to the undeformed plate axis.

2.3 Piezo-electric patch modelling

The modelling of the piezoelectric patches follows the formulation proposed in [1] for the vibrations of generic piezoelectric structures. In analogy to the elastic structure, in the region

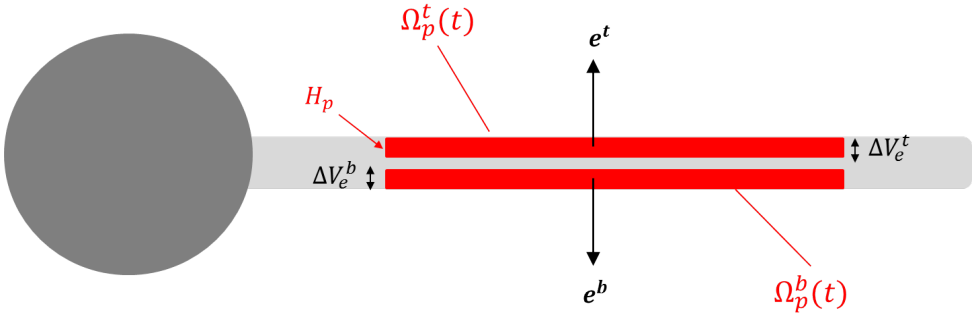

Figure 2: Detailed sketch of the piezoelectric patch configuration.

Ω_p^r, the equations governing the structural displacement are given by

$$\rho \frac{\partial^2 \boldsymbol{\xi}_s}{\partial t^2} - \boldsymbol{\nabla} \cdot \boldsymbol{\sigma}_s(\boldsymbol{\xi}_s, V_e) = \mathbf{0}, \tag{11}$$

where the Cauchy stress tensor $\boldsymbol{\sigma}_s(\boldsymbol{\xi}_s, V_e)$ is modified in order to take into account the electro-mechanical coupling effects. The dependence of the Cauchy stress tensor from the electric potential field V_e within each piezoelectric patch is now explained. In a two-dimensional setting, the generic constitutive equations of a piezoelectric material can be written, using the compact Voigt-Kelvin notation [19], as

$$\begin{pmatrix} \sigma_s^{xx} \\ \sigma_s^{yy} \\ \sigma_s^{xy} \end{pmatrix} = C^e \begin{pmatrix} \varepsilon_{xx} \\ \varepsilon_{yy} \\ 2\varepsilon_{xy} \end{pmatrix} - D^T \begin{pmatrix} \dfrac{\partial V_e}{\partial x} \\ \dfrac{\partial V_e}{\partial y} \end{pmatrix}, \tag{12}$$

$$\begin{pmatrix} d_x \\ d_y \end{pmatrix} = D \begin{pmatrix} \varepsilon_{xx} \\ \varepsilon_{yy} \\ 2\varepsilon_{xy} \end{pmatrix} + E^\epsilon \begin{pmatrix} \dfrac{\partial V_e}{\partial x} \\ \dfrac{\partial V_e}{\partial y} \end{pmatrix}. \tag{13}$$

In the above equations $\boldsymbol{d} = \{d_x, d_y\}^T$ is the dielectric field while C^e is the elastic tensor at constant electric field $\boldsymbol{e} = \boldsymbol{\nabla} V_e$, E^ϵ the permittivity tensor at constant mechanical stress and D the piezoelectric coupling tensor which can be expressed in matrix form as follows

$$D = \begin{bmatrix} 0 & 0 & d_{xy} \\ d_{xy} & d_{yy} & 0 \end{bmatrix}. \tag{14}$$

In our investigation we consider an ideal piezoelectric material that has the same mechanical and inertial properties of the solid structure, i.e. C^e and ρ_s have the same values of the elastic structure material. This allows us to focus the analysis on the pure electro-mechanical coupling effects and their interactions with the stability properties of the fluid-structure system.

In addition to the momentum equation (11), the charge conservation equation has also to be introduced

$$\boldsymbol{\nabla} \cdot \boldsymbol{d}(V_e, \boldsymbol{\xi}_s) = 0. \tag{15}$$

No volume free electric charges are prescribed in the solid region, since at the electric equilibrium, for classical homogeneous piezoelectric materials, the free charges are always concentrated on the boundaries, in the form of surface densities. The above equations are made non-dimensional consistently with the adopted normalization for the fluid-structure equations. In

particular, for the electric potential we assume a reference scale given by $V_e^0 = C_{xx}^e \rho_f U_\infty^2 D/d_{xy}$, where C_{xx}^e is the Young's modulus of the elastic material.

With reference to the configuration illustrated in Figure 2 we assume that the piezoelectric patches are polarized only in their transverse direction ($e_x = \partial V_e/\partial x = 0$) and the electric fields are uniform in the piezoelectric patches, thus $e_y = \partial V_e/\partial y = \Delta V_e/H_p$, where $H_p = 0.02$ denotes the piezoelectric patch thickness and ΔV_e is the electric potential difference between the top and bottom surfaces of one patch. Under such assumptions, only two electro-mechanical couplings can be considered: a d_{yy} coupling (between the transverse electric field e_y and the stress/strain component in the same direction $\sigma_s^{yy}/\varepsilon_{yy}$) and a d_{xy} coupling (between the transverse electric field and the membrane stresses/strains $\sigma_s^{xx}/\varepsilon_{xx}$). In the present study only the d_{xy} coupling is considered. By introducing Eq. (12) in Eq. (11) and Eq. (13) in Eq. (15), after spatially discretising, the governing equations of the elastic plate equipped with the two piezoelectric patches can be written as follows

$$\begin{aligned} M\frac{d^2\mathbf{\Phi}}{dt^2} + K\mathbf{\Phi} - K_p^t\Delta V_e^t - K_p^b\Delta V_e^b &= \mathbf{0}, \\ (K_p^t)^T\mathbf{\Phi} + C_p^t\Delta V_e^t &= Q_e^t, \\ (K_p^b)^T\mathbf{\Phi} + C_p^b\Delta V_e^b &= Q_e^b, \end{aligned} \tag{16}$$

where $\mathbf{\Phi}$ denotes the vector of structural displacement dofs, i.e. the discrete form of $\boldsymbol{\xi}_s$, while ΔV_e^t and ΔV_e^b denote the electric potential difference across the top and bottom piezo-patches. It is recalled that the notation $(\cdot)^t$ and $(\cdot)^b$ denote quantities related to the *top* and to the *bottom* piezo-patches, respectively, as illustrated in Figure 2. Correspondingly, Q_e^t and Q_e^b denote the free electric charges at the piezo-connectors. M and K represent the structural mass and stiffness matrices of the piezoelectric structure, while C_p^t and C_p^b are the equivalent electric capacitance of the two piezo-patches and K_p^t, K_p^b the corresponding electro-mechanical coupling matrices which depend on d_{xy}, on the patch geometry and on the poling direction. With the adopted normalization their non-dimensional values are completely determined by the electro-mechanical coupling coefficient k_e of the piezoelectric material which can be defined for the d_{xy} coupling as follows:

$$k_e^2 = \frac{d_{xy}^2}{C_{xx}^e E_{yy}}, \tag{17}$$

where E_{yy} denotes the piezoelectric material permittivity. k_e^2 can be interpreted as a ratio between the stored electrical energy within the piezo-patches and the mechanical energy in input, thus it is a measure of the electro-mechanical coupling efficiency.

By connecting the two patches in parallel, $\Delta V_e^t = \Delta V_e^b = \Delta V_e$, the system (18) is reduced to

$$\begin{aligned} M\frac{d^2\mathbf{\Phi}}{dt^2} + K\mathbf{\Phi} - K_p\,\Delta V_e &= \mathbf{0}, \\ K_p^T\mathbf{\Phi} + C_p\,\Delta V_e &= Q_e, \end{aligned} \tag{18}$$

with $K_p = K_p^t + K_p^b$, $C_p = C_p^t + C_p^b$ and $Q_e = Q_e^t + Q_e^b$. Since the two piezoelectric patches have the same electro-mechanical properties and are symmetrically placed with respect to the plate axis but with opposite poling directions, i.e. $\mathbf{e}_y$ and $-\mathbf{e}_y$ (where $\mathbf{e}_y$ is the unit vector of the y axis) a uniform σ_s^{xx} distribution does not produce any electric response, i.e. $K_p^T\mathbf{\Phi} = 0$ when $\mathbf{\Phi}$ corresponds to pure traction-compression of the plate. Indeed the electro-mechanical coupling

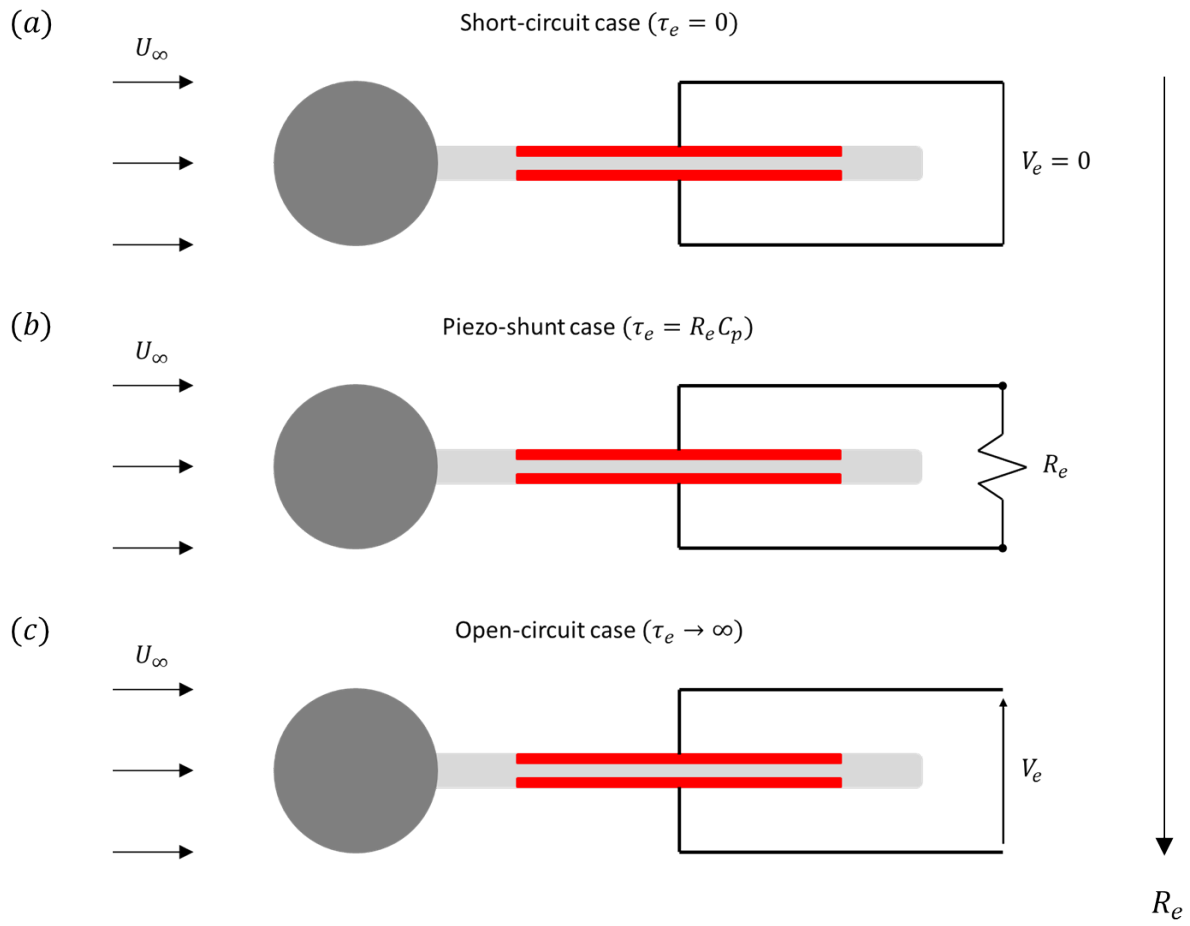

Figure 3: Sketch of (a) the short-circuit configuration, (b) the piezo-shunt configuration and (c) the open-circuit configuration.

becomes effective only for a bending state, for which the σ_s^{xx} distribution is anti-symmetric with respect to the x-axis.

The passive control of the elastic plate deformation is investigated by considering the so-called R-shunt configuration, which is obtained by connecting the two patches to an electrical resistance R_e, as illustrated in Figure 3(b). The electric charge Q_e is then governed by the first-order equation

$$\frac{dQ_e}{dt} + \frac{1}{\tau_e} Q_e = 0, \tag{19}$$

where $\tau_e = R_e C_p$ is the *characteristic electric time* of the equivalent RC circuit. For a fixed value of C_p, the electric time is varied by changing the electrical resistance R_e. For very small values of the resistance, i.e. $\tau_e \to 0$, the electro-mechanical coupling becomes negligible. This corresponds to the *short-circuit* configuration shown in Figure 3(a), for which the two piezoelectric patches are connected each other and the electric potential difference vanishes $\Delta V_e = 0$. On the opposite, for very large values of the resistance, i.e. $\tau_e \to \infty$, the electromechanical coupling is maximal. This corresponds to the *open-circuit* configuration shown in Figure 3(c), for which the electric current in the circuit vanishes $dQ_e/dt \to 0$. It is worthwhile to note that, since the piezoelectric patches have the same mechanical and inertial properties of the elastic plate, in the short-circuit case, where the electro-mechanical coupling is negligible, the pure fluid-mechanical behaviour of the system is recovered.

2.4 Linear global stability of the fluid-solid-electric system

The coupled nonlinear fluid-solid-electric equations introduced so far can be summarized in abstract form as follows

$$\begin{aligned}
\mathcal{B}_f \frac{\partial \boldsymbol{q}_f}{\partial t} - \mathcal{R}_f(\boldsymbol{q}_f, \boldsymbol{q}_e) &= \boldsymbol{0}, \quad \text{on } \Omega_f^r \\
\mathcal{R}_e(\boldsymbol{q}_e) &= \boldsymbol{0}, \quad \text{on } \Omega_f^r \\
\mathcal{B}_s \frac{\partial \boldsymbol{q}_s}{\partial t} - \mathcal{R}_s(\boldsymbol{q}_s, \boldsymbol{q}_p) &= \boldsymbol{0}, \quad \text{on } \Omega_s^r \\
\mathcal{B}_p \frac{d \boldsymbol{q}_p}{dt} - \mathcal{R}_p(\boldsymbol{q}_p, \boldsymbol{q}_s) &= \boldsymbol{0},
\end{aligned} \tag{20}$$

where $\boldsymbol{q}_f$, $\boldsymbol{q}_e$, $\boldsymbol{q}_s$ and $\boldsymbol{q}_p$ denote the partitions of the total system state $\boldsymbol{q} = \{\boldsymbol{q}_f, \boldsymbol{q}_e, \boldsymbol{q}_s, \boldsymbol{q}_p\}^T$ associated with the fluid, the extension, the solid and the electric variables, respectively:

$$\boldsymbol{q}_f = \begin{pmatrix} \boldsymbol{u} \\ p \end{pmatrix}, \qquad \boldsymbol{q}_e = \begin{pmatrix} \boldsymbol{\xi}_f \\ \partial \boldsymbol{\xi}_f / \partial t \end{pmatrix}, \quad \boldsymbol{q}_s = \begin{pmatrix} \boldsymbol{\xi}_s \\ \partial \boldsymbol{\xi}_s / \partial t \end{pmatrix}, \qquad \boldsymbol{q}_p = \begin{pmatrix} Q_e \\ V_e \end{pmatrix}. \tag{21}$$

Using a more compact notation the system (20) can be further rewritten as

$$\mathcal{B} \frac{\partial \boldsymbol{q}}{\partial t} = \mathcal{R}(\boldsymbol{q}). \tag{22}$$

The onset of a coupled fluid-solid-electric instability is then investigated by performing a modal analysis of the linearised perturbations evolving on the top of the steady solution $\boldsymbol{q}_B$ of the nonlinear governing equations, i.e.

$$\mathcal{R}(\boldsymbol{q}_B) = \boldsymbol{0}. \tag{23}$$

For such purpose the total solution $\boldsymbol{q}(\boldsymbol{X},t)$ of Eq. (20) is decomposed as follows

$$\boldsymbol{q}(\boldsymbol{X},t) = \boldsymbol{q}_B(\boldsymbol{X}) + \epsilon \boldsymbol{q}'(\boldsymbol{X},t), \tag{24}$$

and by assuming $\epsilon \ll 1$, at the first order in ϵ a system of linear equations for the total perturbation field $\boldsymbol{q}'(\boldsymbol{X},t)$ is obtained from Eq. (20):

$$\mathcal{B}\frac{\partial \boldsymbol{q}'}{\partial t} = \left.\frac{\partial \mathcal{R}(\boldsymbol{q})}{\partial \boldsymbol{q}}\right|_{\boldsymbol{q}_B} \boldsymbol{q}'. \tag{25}$$

The linearised dynamics of the fluid-solid-electric system can be conveniently investigated by casting the perturbation field in the normal form $\boldsymbol{q}'(\boldsymbol{X},t) = \hat{\boldsymbol{q}}(\boldsymbol{X})e^{\lambda t}$, which yields the following global eigenvalue problem for the global mode $\hat{\boldsymbol{q}}(\boldsymbol{X})$ and the associated eigenvalue $\lambda = \sigma + \imath\omega \in \mathbb{C}$:

$$\lambda \mathcal{B}\hat{\boldsymbol{q}} = \mathcal{A}\hat{\boldsymbol{q}}. \tag{26}$$

A global instability clearly arises when $\sigma > 0$ for some values of the governing parameters. In addition, we have introduced the following notation for the Jacobian operator $\mathcal{A} = \partial\mathcal{R}(\boldsymbol{q})/\partial\boldsymbol{q}|_{\boldsymbol{Q}_b}$ which can be formally represented as

$$\mathcal{A} = \begin{pmatrix} \mathcal{A}_{ff} & \mathcal{A}_{fe} & \mathcal{I}_{fs} & 0 \\ 0 & \mathcal{A}_{ee} & \mathcal{I}_{es} & 0 \\ \mathcal{I}_{fs} & 0 & \mathcal{A}_{ss} & \mathcal{A}_{sp} \\ 0 & 0 & \mathcal{A}_{ps} & \mathcal{A}_{pp} \end{pmatrix}. \tag{27}$$

In particular the term $\mathcal{A}_{fe}$ results from the linearisation of the geometric nonlinearities of the ALE mapping in the Navier-Stokes equations (6), while $\mathcal{A}_{sp}$ and $\mathcal{A}_{ps}$ express the electromechanical coupling due to the presence of the piezo-patches. Finally the notation $\mathcal{I}$ has been used for the coupling terms due to the boundary conditions of the fluid-structure and extension problem at Γ^r_{FS}.

3 NUMERICAL DISCRETISATION

The coupled systems of nonlinear and linearised fluid-solid-electric equations, Eqs. (20) and (25), are numerically discretized by means of a finite element method on unstructured grids made of triangular elements using the open-source library FreeFem++[17]. The employed grids are represented in Figure 4: a local mesh size of 0.01 is adopted on the structure wall and within the plate, with a total of six triangles along the plate thickness and two triangles being used for the discretisation of each piezoelectric patch. The fluid domain size is of $[40, 75] \times [40, 40]$. Classical $\mathbb{P}_2$-$\mathbb{P}_1$ Taylor-Hood elements are used to represent the fluid velocity and pressure. Both the the fluid mesh and the solid displacement are also represented by means of $\mathbb{P}_2$ elements. The kinematic and equilibrium boundary conditions at the fluid-structure interface Eq. (10) are treated by means of a Lagrange multiplier approach, with the Lagrange multipliers functions being discretised by means of $\mathbb{P}_1$ elements, consistently with the well established *inf-sup* condition. The same approach is also adopted for the boundary conditions of the extension problem on Γ^r_{FS}. The total number of triangles is of 35651 with a corresponding total number of dofs for $\boldsymbol{q}$ of 441365. A classical Newton algorithm is used for the computation of the base solution $\boldsymbol{q}_B$. All the required matrix inversions are handled by means of the sparse direct-solver MUMPS[16] while the involved large-scale eigenvalue problems are solved using the Arnoldi algorithm implemented in the ARPACK library[15], with a shift-invert transformation.

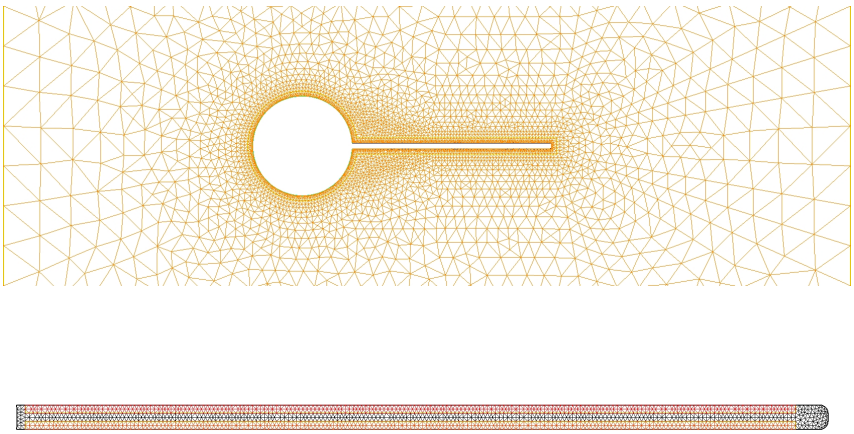

Figure 4: Detail view of the employed computational grids: near body fluid mesh (top) and elastic plate mesh (bottom). The red regions of the elastic plate mesh correspond to the modeled piezoelectric patches.

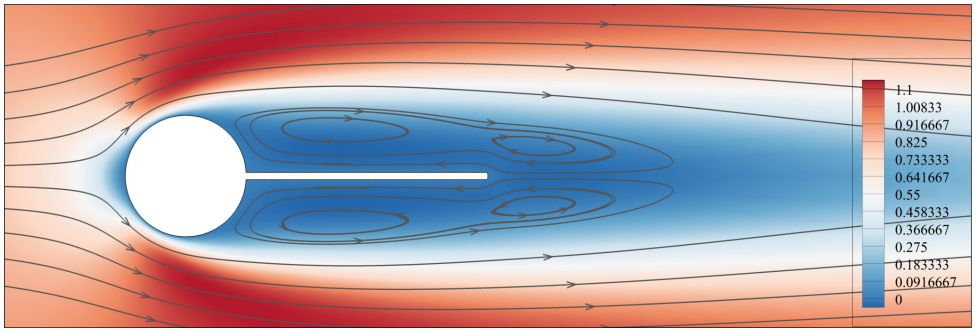

Figure 5: Steady base flow solution: velocity modulus $\|\boldsymbol{u}\|$ and superposed streamlines.

4 RESULTS

4.1 Fluid-solid-electric stability analysis

As already mentioned, the considered value of the fluid-structure parameters are given by $Re = 80$, $\rho = 50$ and a bending stiffness of the elastic plate $K = 0.3$ while for the piezoelectric material we assume an electro-mechanic coupling coefficient $k_e = 0.57$. The flow field corresponding to the base equilibrium solution $\boldsymbol{q}_B$ is illustrated in Figure 5 by means of the modulus of $\boldsymbol{u}_B$ featuring a symmetric structure with respect to the horizontal axis. In the same figure the recirculating flow structures which develop in the wake of the solid body are illustrated by means of the flow streamlines: four symmetric recirculation bubbles are observed, two being attached to elastic plate and the remaining two located behind it on the upper and lower sides. Due to these recirculating flow structures, the elastic plate is subject to a compression stress field which applies on Γ_{FS}. However the corresponding displacements are very small, with a maximum x displacement of $\mathcal{O}(10^{-6})$, so that the deformed configuration can be well approximated by the undeformed one, which is consistent with the linear small deformation assumption for the structure modelling introduced in Section 2.2.

The linear stability of the steady solution $\boldsymbol{q}_B$ is first analysed by examining the eigenvalue spectrum, Figure 6, of the fluid-structural system without any electro-mechanical coupling (blue dots), which is equivalent to the short-circuit configuration. An unstable oscillatory mode is

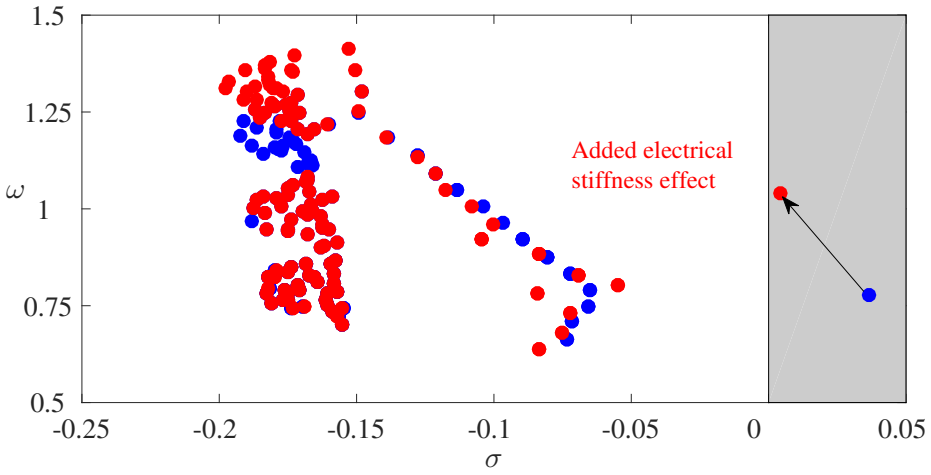

Figure 6: Eigenvalue spectrum of the pure fluid-structure system (blue dots) and the fluid-solid-electric system with piezo-patches in open circuit (red dots).

observed, with a circular frequency of ≈ 0.75. By introducing the piezoelectric patches in an open-circuit configuration (red dots), the leading mode is damped, but remains still unstable, while its frequency is increased.

The spatial shape and temporal behaviour of the pure fluid-structural mode and its fluid-solid-electric counterpart are compared in Figure 7, which depicts the real streamwise component of the complex velocity field. The low-frequency unstable mode, obtained for the short-circuit configuration, is shown in the right column panels. It exhibits an oscillatory pattern, typical of globally unstable wakes with a growing amplitude while moving downstream. The associated elastic plate motion, characterised by a single-node bending mode, has a weak amplitude. The spatial shape of the higher-frequency unstable mode, obtained when the piezoelectric coupling is introduced (open-circuit configuration), is significantly modified. Since the frequency of the mode is higher than in the short-circuit case, the spatial wavenumber of its oscillatory pattern is increased. Compared to the low-frequency mode, the modal y displacement of the plate trailing edge is three order of magnitude greater for the high-frequency mode (when the same normalization is used for both the modes) thus indicating that the structural motion has an higher amplitude in the fluid-solid-electric case. Interestingly, for this mode, the largest magnitude of the fluid velocity are obtained close to the elastic plate and the bending shape of the elastic plate is changed.

A first attempt to understand why the electro-mechanical coupling have a damping effect on the leading mode and produces a shift of its frequency is to re-examine Eq.(18). For the open-circuit configuration, the free charge vanishes $Q_e = 0$ and the electric potential can be obtained as $\Delta V_e = -C_p^{-1} K_p^T \mathbf{\Phi}$. By introducing this expression in the first equation of Eq. (18), we get

$$M\frac{d^2\mathbf{\Phi}}{dt^2} + (K + K_p C_p^{-1} K_p)\mathbf{\Phi} = \mathbf{0}, \tag{28}$$

which clearly shows that the piezoelectric patches act as an added stiffness $K_p C_p^{-1} K_p$ in the solid dynamics, without changing the inertial or elastic properties of the structure.

4.2 Piezo-shunts configuration

To further understand how the leading mode is shifted in the eigenvalue spectrum, we consider the piezo-shunt configuration where the electrical resistance R_e is added to connect the

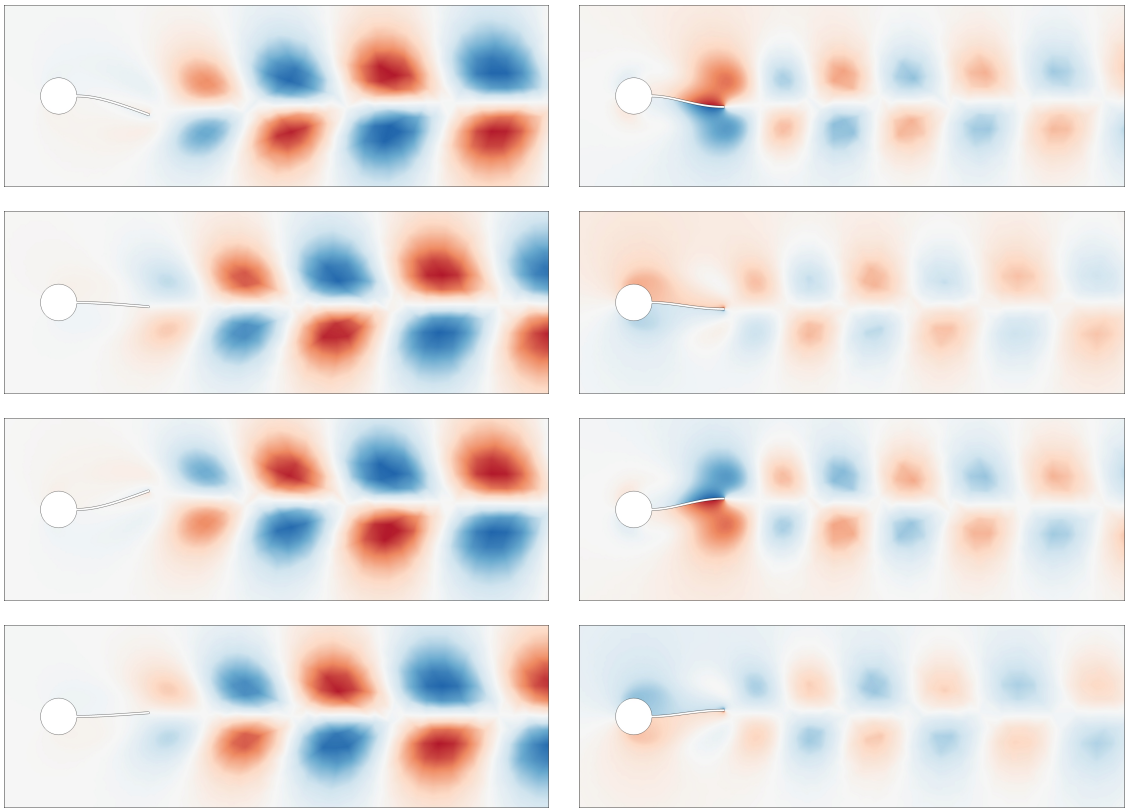

Figure 7: Space-time evolution of the global modes of the fluid-solid-electric system: short-circuit case (left column) and open-circuit case (right column). For each mode the real streamwise component of the velocity field and the corresponding plate displacement are depicted at different phases ϕ: $\phi = 0$ (first row), $\phi = \pi/2$ (second row), $\phi = \pi$ (third row) and $\phi = 3\pi/2$ (fourth row).

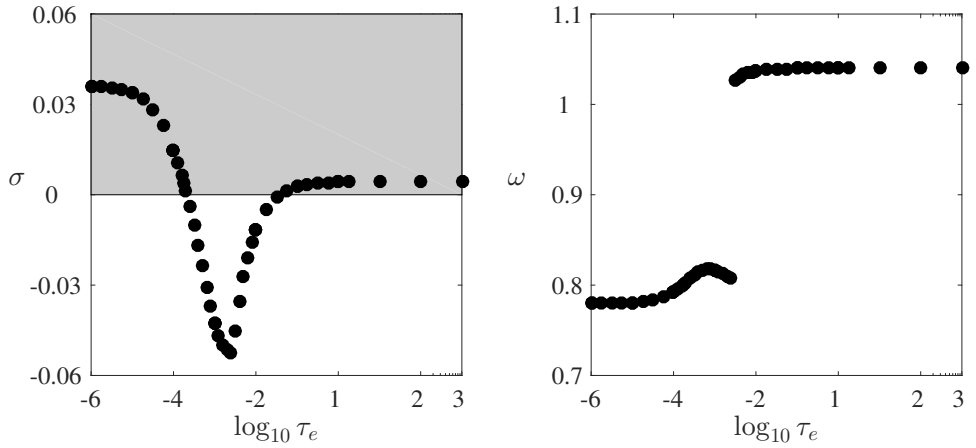

Figure 8: Growth rate (left panel) and frequency (right panel) of the leading eigenmode of the fluid-solid-electric system as a function of $\tau_e = R_e C_p$, the electric time.

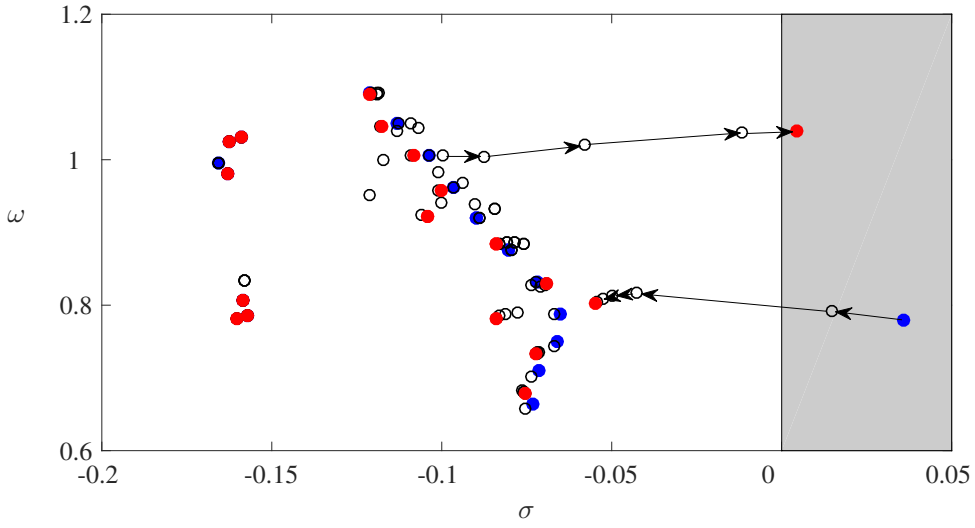

Figure 9: Eigenvalue path of two modes in the complex plane while varying the value of τ_e. Blue dots denote the spectrum obtained for $\tau_e = 10^{-5}$ while the red dots denote the spectrum obtained for $\tau_e = 10^3$.

two piezoelectric patches. By varying R_e between 0 and ∞, we progressively change from the short-circuit configuration (fluid-structure) to the open-circuit configuration. In the following, we will rather use the time $\tau_e = R_e C_p$ to describe the results, since the value of C_p is unchanged.

The growth rate and frequency of the leading eigenvalue are plotted in Figure 8 as a function of τ_e varying in the range $[10^{-5}, 10^3]$. There exists a finite range of values $2.12 \times 10^{-4} \lesssim \tau_e \lesssim 0.04$ for which the leading eigenmode is stabilized and thus the flutter instability is completely suppressed. In this range, the frequency of the leading mode, Figure 8(right), suddenly jumps from $\omega \approx 0.78$ to $\omega \approx 1.04$, suggesting that the unstable modes in the short-circuit and open-circuit configurations are two different modes.

To confirm this, the path of these two modes have been tracked in the complex plane as shown in Figure 9. When increasing τ_e, the pure fluid-structure mode (blue dot) is increasingly damped, moving to the left half of the complex plane. At the same time, a higher frequency mode belonging to the least damped branch is progressively destabilized and gets unstable for $\tau_e = 10^3$.

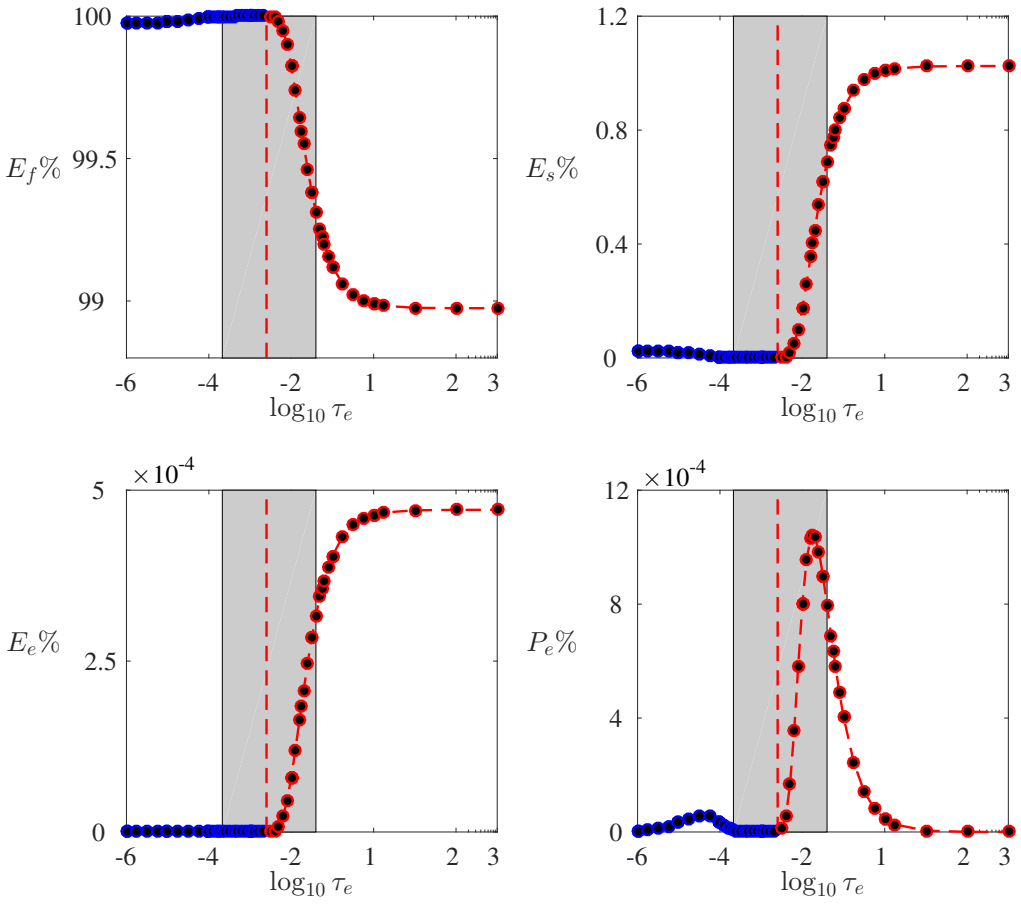

Figure 10: Passive control using piezo-shunt: analysis of the system energy distribution and dissipation while varying τ_e. Top-left: fluid energy E_f. Top-right: structure energy E_s. Bottom-left: electric energy E_e. Bottom-right: dissipated electric power P_e. All quantities are reported as a percentage of the total system energy. The gray shaded area denotes the range of stabilizing values of τ_e.

To better characterize the dynamics associated with these two modes, an analysis of the energetic distribution in the modes is performed. The following quantities are introduced:

$$E_f = \frac{1}{2}\int_{\Omega_f} \|\hat{\boldsymbol{u}}\|^2, \tag{29}$$

$$E_s = \frac{1}{2}\int_{\Omega_s} \rho_r |\lambda|^2 \|\hat{\boldsymbol{\xi}}_s\|^2 + \frac{1}{2}\int_{\Omega_s} \varepsilon(\hat{\boldsymbol{\xi}}_s)^* : C^e : \varepsilon(\hat{\boldsymbol{\xi}}_s), \tag{30}$$

$$E_e = \frac{1}{2} C_p \|\hat{V}_e\|^2, \qquad P_e = \frac{2E_e}{\tau_e}, \tag{31}$$

E_f denotes the mean kinetic energy in the fluid over a period $T = 2\pi/\omega$, where ω is the frequency of the mode. E_s is the mean structural energy, E_e the stored electric energy and P_e the dissipated electric power. The results obtained when considering the leading mode are depicted in Figure 10 as a function of τ_e. Note that, whatever the value of τ_e, the largest part of the energy is stored in the fluid, with $E_f \gtrsim 99\%$ of the total system energy. Interestingly, for small values of τ_e, the percentage of energy in the solid or in the electric circuit is almost negligible. This indicates that the unstable mode of the short-circuit configuration (the fluid-structure mode) is mainly driven by the fluid dynamics. On the other hand, for large values of τ_e, the percentage of structural and electric energy significantly increases, thus indicating that the destabilized mode is driven by the electro-structural dynamics.

Concerning the behaviour of P_e, it is relevant only for the high frequency mode (red portion of the curve) displaying a peak which occurs within the stabilizing range of τ_e values. Nevertheless this peak does not correspond to the value of τ_e for which a maximum damping of the leading mode is obtained.

5 CONCLUSIONS

A fluid-solid-electric stability analysis has been used to assess the performance of piezoelectric patches in suppressing vibrations of a flexible plate clamped at the rear of a rigid cylinder and immersed in a viscous flow. In the nominal configuration, i.e. without piezoelectric patches, an unstable mode is obtained which explains the onset of the plate's deformation. An energetic analysis has shown that this mode is mainly driven by the fluid dynamics: the small bending oscillation amplitude is induced by the fluid vortex-shedding. When increasing values of the electrical resistance in piezo-shunt configurations, this mode is damped and even stabilised for large enough resistance, proving the efficiency of this passive control. However, when too large values of the resistance are considered, a second mode, characterized by higher-frequency and larger bending amplitudes, is destabilised. This "waterbed effect" of the passive control may be due to the underlying assumption of identical mechanical properties for the elastic structures and the piezoelectric patches. To complete the preliminary results shown in this paper, we plan to vary the elastic parameters (density ratio and bending stiffness) and determine whether this electric passive control remains efficient for stabilizing other types of fluid/structure modes, as static (divergent) modes or oscillating modes with higher wave numbers.

Acknowledgement

This project has received funding from the European Research Council (ERC) under the European Union's Horizon 2020 research and innovation programme (grant agreement No 638307).

REFERENCES

[1] O. Thomas, J.-F. Deü and J. Ducarne. Vibrations of an elastic structure with shunted piezoelectric patches: efficient finite element formulation and electromechanical coupling coefficients. *International Journal for Numerical Methods in Engineering* **80**:235–268, 2009.

[2] O. Thomas, J. Ducarne and J.-F. Deü. Performance of piezoelectric shunts for vibration reduction. *Smart Materials and Structures* **21**:015008, 2012.

[3] J. J. Allen and A. J. Smits, Energy harvesting eel, *Journal of Fluids and Structures*, **15**:1–12, 2001.

[4] Y. Yu and Y. Liu, Flapping dynamics of a piezoelectric membrane behind a circular cylinder, *Journal of Fluids and Structures*, **55**:347–363, 2015.

[5] S. Michelin and O. Doare, Energy harvesting efficiency of piezoelectric flags in axial flows, *Journal of Fluid Mechanics*, **714**:489–594, 2013.

[6] D. T. Akcabay and Y. L. Young, Hydroelastic response and energy harvesting potential of flexible piezoelectric beams in viscous flow, *Physics of Fluids*, **24**:054106, 2012.

[7] D. Sipp, O. Marquet, P. Meliga and A. Barbagallo, Dynamics and control of global instabilities in open-flows: a linearized approach, *Applied Mechanics Reviews*, **63**:030801, 2010.

[8] O. Marquet, D. Sipp and L. Jacquin, Sensitivity analysis and passive control of cylinder flow, *Journal of Fluid Mechanics*, **615**:221–252, 2008.

[9] O. Doare and S. Michelin, Piezoelectric coupling in energy-harvesting fluttering flexible plates: linear stability analysis and conversion efficiency, *Journal of Fluids and Structures*,**27**, Issue 8:1357–1375, 2011.

[10] J. Lee and D. You., Study of vortex-shedding-induced vibration of a flexible splitter plate behind a cylinder. *Physics of Fluids*, **25**:110811, 2013.

[11] M. A. Fernandez and P. Le Tallec, Linear stability analysis in fluid-structure interaction with transpiration. Part I: Formulation and mathematical analysis, *Computer Methods in Applied Mechanics and Engineering*, **192**:4805-4835, 2003.

[12] M. A. Fernandez and P. Le Tallec, Linear stability analysis in fluid-structure interaction with transpiration. Part II: Numerical analysis and applications, *Computer Methods in Applied Mechanics and Engineering*, **192**:4837–4873, 2003.

[13] S. Bagheri, A. Mazzino, and A. Bottaro. Spontaneous symmetry breaking of a hinged flapping filament generates lift. *Physical Review Letters* **109**:154502, 2012.

[14] J. Donea, S. Giuliani, and J.-P. Halleux. An arbitrary Lagrangian-Eulerian finite element method for transient dynamic fluid-structure interactions. *Computer methods in applied mechanics and engineering* **33**: 689-723, 1982.

[15] R. B. Lehoucq, D. C. Sorensen, and C. Yang, *ARPACK Users Guide: Solution of Large-Scale Eigenvalue Problems with Implicitly Restarted Arnoldi Methods*, siam ed. (1998).

[16] R. Amestoy, I. Duff, and J.-Y. LExcellent, *Multifrontal parallel distributed symmetric and unsymmetric solvers*. Comput. Methods Appl. Math. **184**, 501520

[17] *Source code and documentation available at http://www.freefem.org (2017)*.

[18] K. Stein, T. Tezduyar, and R. Benney, Mesh moving techniques for fluid-structure interactions with large displacements. *ASME Journal of Applied Mechanics* **70**, 5863, 2003.

[19] J. N., Reddy. Mechanics of laminated composite plates. *CRC press*, 1997.

[20] Z., Yu, A DLM/FD method for fluid/flexible-body interactions. *J. Comp. Phys.*, **207**:1–27, 2005.